

Local shear transformations in deformed and quiescent hard-sphere colloidal glasses

K. E. Jensen*

Department of Physics, Harvard University, Cambridge, Massachusetts 02138, USA

D. A. Weitz

*Department of Physics, Harvard University, Cambridge, Massachusetts 02138, USA
and School of Engineering and Applied Sciences, Harvard University, Cambridge, Massachusetts 02138, USA*

F. Spaepen†

School of Engineering and Applied Sciences, Harvard University, Cambridge, Massachusetts 02138, USA

(Received 15 May 2014; published 10 October 2014)

We perform a series of deformation experiments on a monodisperse, hard-sphere colloidal glass while simultaneously following the three-dimensional trajectories of roughly 50 000 individual particles with a confocal microscope. In each experiment, we deform the glass in pure shear at a constant strain rate $[(1-5) \times 10^{-5} \text{ s}^{-1}]$ to maximum macroscopic strains (5%–10%) and then reverse the deformation at the same rate to return to zero macroscopic strain. We also measure three-dimensional particle trajectories in an identically prepared quiescent glass in which the macroscopic strain is always zero. We find that shear transformation zones exist and are active in both sheared and quiescent colloidal glasses, revealed by a distinctive fourfold signature in spatial autocorrelations of the local shear strain. With increasing shear, the population of local shear transformations develops more quickly than in a quiescent glass and many of these transformations are irreversible. When the macroscopic strain is reversed, we observe partial elastic recovery, followed by plastic deformation of the opposite sign, required to compensate for the irreversibly transformed regions. The average diameter of the shear transformation zones in both strained and quiescent glasses is slightly more than two particle diameters.

DOI: [10.1103/PhysRevE.90.042305](https://doi.org/10.1103/PhysRevE.90.042305)

PACS number(s): 82.70.Dd, 81.05.Kf, 62.20.F–

I. INTRODUCTION

When an external stress is applied to a material, it deforms: first elastically (reversibly) and then plastically (irreversibly) when strained beyond the yield point. While the mechanisms of deformation in crystalline materials have been well understood for decades, a similar understanding of the deformation mechanisms in amorphous materials remains a topic of intense research. Theory [1–4] and simulation [5–9] predict the existence of flow defects or shear transformation zones that govern plastic deformation in glasses as dislocations do in crystals. However, unlike dislocations, which are readily observable as defects in an otherwise-regular crystal structure, the corresponding entities in glasses are difficult to observe directly in the amorphous structure and a full understanding of their nature and origin is lacking. This insight is particularly important for understanding the deformation and failure mechanisms of bulk metallic glasses, a relatively new class of strong materials that show considerable promise for structural applications [10].

An ideal experiment to investigate deformation mechanisms in a glass would simultaneously follow the microscopic and macroscopic dynamics during quasistatic deformation. In atomic and molecular glasses, however, the constituent elements are simply too small and move too quickly for this ideal experiment to be possible. Colloidal glasses provide

unique experimental systems for probing the structure and dynamics of glasses over the complete range of length scales from the individual colloidal particles up to the bulk amorphous material [11,12]. Monodisperse, hard-sphere colloidal particles can easily be made to form glasses by sedimentation onto flat or patterned substrates, with the resulting structure dependent on the deposition flux and the boundary condition imposed by the substrate [13]. The relative ease of both structure formation and detailed observation in three dimensions using optical microscopy makes colloidal glasses ideal for studying structure-property relations in a generic amorphous solid. Experiments on the deformation of hard-sphere colloidal crystals proved to be in excellent agreement with classical dislocation theory [14–18], which gives us confidence that these systems provide a reliable scaled-up picture of phenomena on the atomic level.

Experiments on hard-sphere colloidal glasses under shear deformation [11,19] identified shear defects as localized regions of high irreversible strain and concluded that they can be described by Eshelby's analysis [20,21] of a highly strained inclusion coupled to an elastic isotropic surrounding medium. For a shear transformation of a spherical inclusion of radius a with unconstrained transformation shear strain $\epsilon_{yz}^T = \gamma/2$ and the same elastic properties as its surroundings, the shear strain field in the y - z plane is

$$\epsilon_{yz}(\mathbf{r}) = \begin{cases} \epsilon_{yz}^0, & r < a \\ \frac{\epsilon_{yz}^0 a^3}{4r^5} [9a^2 c - (2+3c)r^2 - 15c(7a^2 - 5r^2) \cos(4\theta)], & r \geq a, \end{cases} \quad (1)$$

*Present address: Department of Mechanical Engineering and Materials Science, Yale University, New Haven, Connecticut 06511, USA; kjensen@post.harvard.edu

†spaepen@seas.harvard.edu

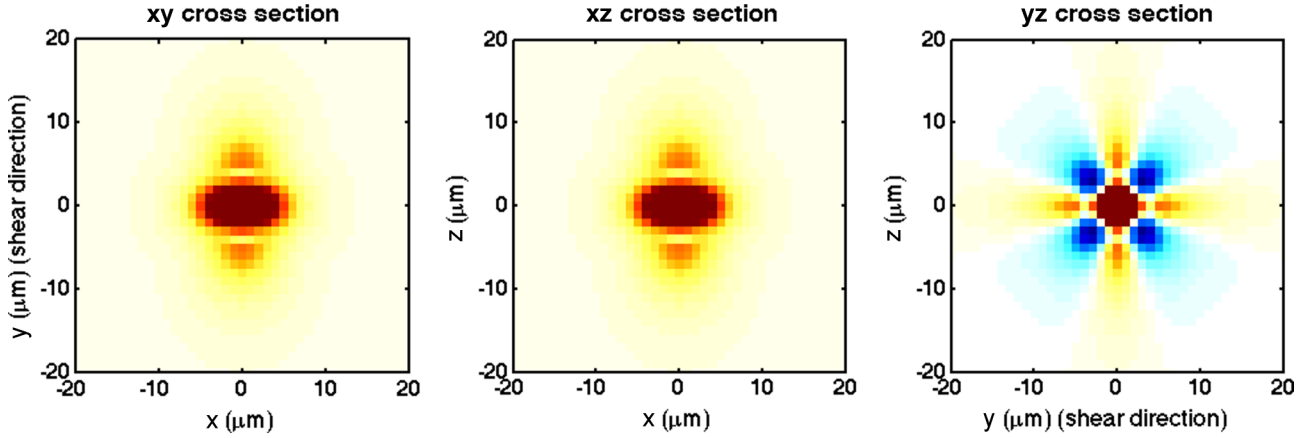


FIG. 1. (Color online) Plots of the (a) x - y , (b) x - z , and (c) y - z cross sections of the 3D spatial autocorrelation function of the ϵ_{yz} analytic strain field for a single ideal Eshelby inclusion of radius $2.25 \mu\text{m}$ embedded in an infinite isotropic elastic medium with Poisson ratio $\nu = 1/3$. This three-dimensional correlation pattern with its characteristic fourfold pattern in the y - z plane is the signature of Eshelby inclusions active in an elastic matrix.

where $c = 1/4(4 - 5\nu)$ is a dimensionless elastic constant, with ν Poisson's ratio, $\mathbf{r}(y, z)$ the position vector with origin at the center of the inclusion, and $\theta = \cos^{-1}(z/r)$. Details of the derivation and the full three-dimensional (3D) expression are given in the Appendix [Eq. (A5)].

The $\cos(4\theta)$ dependence of the strain field outside the inclusion produces a characteristic fourfold pattern in the y - z plane. The presence of this pattern is the signature that Eshelby inclusions are active in the material. Experimentally, the strain field is analyzed by its autocorrelation function. Figure 1 shows the 3D spatial autocorrelation function of the analytic ϵ_{yz} strain field of Eq. (A5) on the three orthogonal coordinate planes. The plot on the y - z plane maintains the characteristic fourfold symmetry. Recent experiments observed this fourfold signature in spatial autocorrelations of local strain measured for a density-matched poly(methyl methacrylate) colloidal glass during steady-state homogenous deformation [19]. The same signature was also recently seen in 2D simulations of supercooled liquids under shear [9].

However, much remains unknown about these shear transformation zones that behave as Eshelby inclusions: Do they exist in the absence of applied strain? How does their population evolve with time and applied strain? What happens to these defects when the macroscopic applied strain is reversed?

Here we show that shear transformation zones are active in both quasistatically sheared and quiescent (i.e., undeformed) colloidal glasses. We confirm that these regions are Eshelby-type shear inclusions. In the absence of applied strain, shear transformation zones are thermally activated in all directions and produce zero macroscopic strain. When a uniform macroscopic shear strain is applied to the glass beyond the yield point, a fraction of these shear defects transforms irreversibly in the direction of the applied shear. When the applied macroscopic strain is reversed, we observe an initial elastic recovery followed by plastic deformation governed by inclusions of the opposite sign until the macroscopic strain has fully returned to zero.

II. EXPERIMENTS

We perform experiments with hard-sphere colloidal silica particles with a polydispersity $< 3.5\%$ and diameter $2R = 1.55 \mu\text{m}$ [22] in a mixture of dimethyl sulfoxide (62.8% by volume), deionized water (36.0% by volume), and fluorescein-NaOH dye solution (1.2% by volume). The particles have nearly twice the density of the surrounding fluid, with a density difference of $\Delta\rho = 0.94 \text{ g/cm}^3$. The Péclet number for sedimentation at room temperature under earth's gravity is $Pe = \Delta\rho g R^4 / k_B T = 0.83$, which means that the rates of sedimentation and diffusion are similar. The dye solution is 3% by weight fluorescein-NaOH in water, which both enables fluorescent imaging of the sample and reduces the Debye screening length of the particles to less than 10 nm. The fluid phase matches the index of refraction of the particles and has a viscosity $\eta = 1.6 \text{ mPa s}$.

We prepare colloidal glasses directly in the sample cell by high-flux sedimentation at $1g$ onto an amorphous template [23], starting from an initial volume fraction ϕ_0 of about 3.5%. These conditions result in a dimensionless deposition flux of $\phi_0 Pe = 0.03$, which corresponds to a very slow quench rate, just high enough to ensure glass formation [13], so that we form as relaxed and low energy a glass as possible. After sedimentation is complete, the colloidal glass has a total thickness of about $250 \mu\text{m}$. The volume fraction at the bottom of the sediment, where the experiment takes place, is $\phi = 62\%$ as measured by particle counting. A radial distribution function $g(R)$ of one of the systems studied is shown in Fig. 2. We verify that there are no crystalline regions anywhere in the sample by directly imaging the entire shear gap throughout the experiment.

We apply deformation to colloidal glasses with a shear apparatus that allows simultaneous three-dimensional imaging of the individual colloidal particles with a confocal microscope. A schematic of the shear apparatus is shown in Fig. 3. The colloid is contained in a cylindrical metal sample reservoir $\sim 1 \text{ cm}$ in diameter that is integrated into the shear apparatus. The reservoir is sealed at the bottom by a

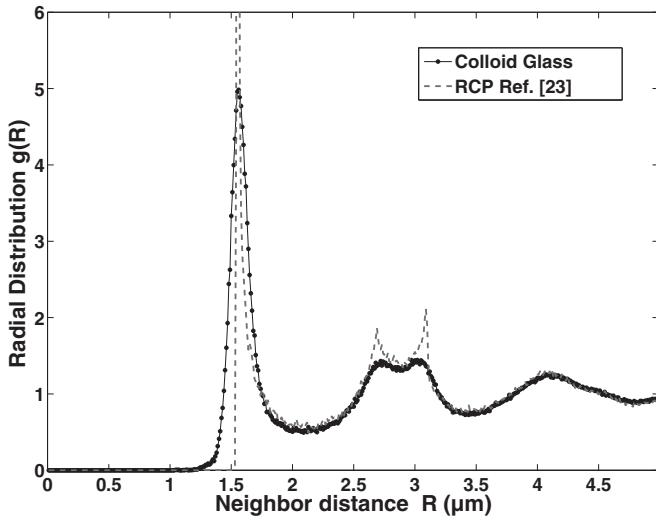


FIG. 2. Radial distribution function $g(R)$ of the colloidal glass (dots). The radial distribution of the random close packing of Finney [24] (dashed line), scaled for the same particle diameter, is shown for comparison.

0.17-mm-thick glass coverslip affixed with glue. This coverslip is microlithographically patterned with an amorphous template etched into the glass that prevents crystallization of the sample during glass formation [23]. The entire shear cell apparatus, including the sample reservoir, is fixed to the microscope stage and does not move over the course of the experiment.

We use a computer-controlled piezoelectric actuator to apply the shear deformation. The actuator has a maximum travel of $80 \mu\text{m}$ in the y direction and an accuracy $\pm 5 \text{ nm}$. It is mechanically coupled to the glass by a perforated hollowed-out metal cylindrical post with a fine gold 300-mesh transmission electron microscope (TEM) grid that spans the bottom of the

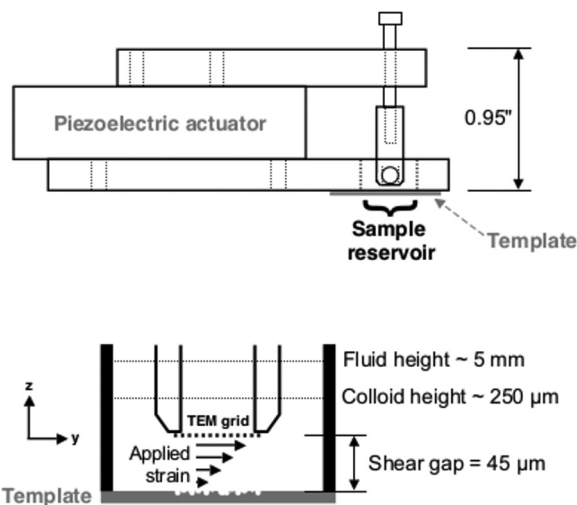


FIG. 3. On the top is the side view of the assembled shear cell, drawn to scale. Shear is applied to a sample in the reservoir with a piezoelectric actuator that is mechanically coupled to the sample via a height-adjustable post. On the bottom is the cross section schematic of the sample reservoir, not to scale. Shear can be applied positively or negatively along the y direction.

post and is embedded in the glass. The TEM grids have a bar width of $10 \mu\text{m}$ and a $73\text{-}\mu\text{m}$ empty spacing between the bars, so the grid does not interfere with the sedimentation process. The height of the grid is adjustable by a No. 2-56 screw that moves the post vertically. The shear gap Δz is the separation between the bottom of the TEM grid and the amorphous template. In the experiments reported here, the gap was $\Delta z = 45 \mu\text{m}$. The maximum available strain rate is about 10^{-2} s^{-1} , limited by the step sizes for the piezo having to be small compared to the particle size and by the maximum communication rate from the computer to the piezo controller. However, because we are interested in homogenous deformation, all of our experiments are conducted well below this upper limit.

The entire shearing setup is assembled and the shear gap geometry fixed prior to the introduction of the initially dilute colloid. Sedimentation is complete within about 2 h, after which the glass is allowed to relax further for 6 h. By quenching the glass directly in the sample cell, we ensure that the glass has never experienced any strain prior to the experiment. This procedure embeds the TEM grid deep inside the sample, about $200 \mu\text{m}$ below the surface of the sediment, ensuring strong contact between the colloidal glass and the grid.

Each deformation experiment consists of a single strain cycle: We apply a uniform macroscopic shear strain to the glass at a strain rate $\dot{\gamma}_{yz}$, up to a maximum macroscopic strain γ_{max} , and then reverse the deformation at an equal, but opposite, strain rate until the macroscopic strain returns to zero. A period of quiescence follows each deformation experiment before the start of the next one. We will focus most of our discussion on a single representative experiment taken from a sequence of five consecutive independent plastic deformation experiments: experiment 1, to $\gamma_{\text{max}} = 5.0\%$ at $\dot{\gamma} = 5.0 \times 10^{-5} \text{ s}^{-1}$; experiment 2, to $\gamma_{\text{max}} = 10.0\%$ at $\dot{\gamma} = 5.0 \times 10^{-5} \text{ s}^{-1}$; experiment 3, to $\gamma_{\text{max}} = 10.0\%$ at $\dot{\gamma} = 2.0 \times 10^{-5} \text{ s}^{-1}$; experiment 4, to $\gamma_{\text{max}} = 5.0\%$ at $\dot{\gamma} = 5.0 \times 10^{-5} \text{ s}^{-1}$ (a repeat of experiment 1); and experiment 5, to $\gamma_{\text{max}} = 5.0\%$ at $\dot{\gamma} = 2.0 \times 10^{-5} \text{ s}^{-1}$. Between each experiment, the glass sample was quiescent for 1000 s, during which time we continued to image the particles. All of these strain rates are slow enough to ensure macroscopically uniform deformation (no shear bands), as confirmed by the strain measurements and direct observation. The maximum macroscopic strains exceed the measured yield point of this colloidal glass, $\gamma_{\text{yield}} \approx 2\%$ [25,26], as well as that of metallic glasses, which are the closest atomic analog [27].

Here we focus on the results of the slowest 10% maximum strain experiment (experiment 3) because this gives us the best time resolution. We additionally include results from the other 10% strain experiment (experiment 2) for the purpose of comparing the effects of strain rate. Finally, we report observations on a quiescent glass to which we never applied strain, but which had otherwise identical preparation and experimental conditions as the deformed glass.

Although the strain we apply is cyclic, it is important to note that these are not oscillatory strain experiments. Oscillatory strain experiments [28–30] and simulations [31–33] typically involve deforming a glass through large numbers of strain cycles toward a steady-state oscillation, also usually at strain rates that are orders of magnitude higher than in our experiments. Our experiments focus on the initial

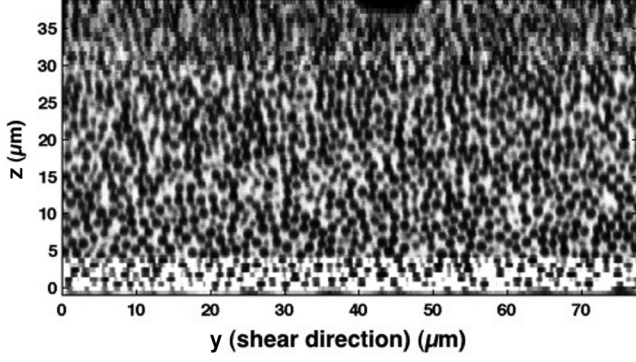


FIG. 4. Example of the confocal raw data, showing the high-resolution central stack ($4.5 \mu\text{m} \leq z \leq 30 \mu\text{m}$) overlaid on the low-resolution stack that spans the entire shear gap from the stationary template to the moving TEM grid. Part of one of the bars of the TEM grid is visible in cross section at the top of the image ($40 \mu\text{m} \leq y \leq 48 \mu\text{m}$). The top of the amorphous template is just visible as dark bumps at the bottom of the image. A video of this cross section in motion during a deformation experiment is available online in Ref. [34].

deformation of a glass at very low quasistatic strain rates and we reverse the strain in order to probe the reversibility of the local deformations.

All samples are imaged from below in three dimensions using a Leica SP5 point-scanning confocal microscope. All image stacks are taken far from the edges of the template and from the sample cell walls to avoid possible boundary effects. During deformation experiments, we take two image stacks at each time step: a low-resolution stack that spans the entire shear gap and a high-resolution image stack in the middle of the shear gap, about $10 \mu\text{m}$ away from either top or bottom of the gap. The low-resolution images allow us to monitor the entire shear gap and verify that there is no slip at either the amorphous template or the TEM grid nor any inhomogeneous shear effects that might change the effective applied strain. The high-resolution stack provides the data that we use for locating the particles and subsequent analyses. Figure 4 shows an example composite y - z cross section through the raw image data, with the high-resolution central region overlaid on the low-resolution stack. It takes about 5.5 min to acquire both stacks and we repeat the scans every 6 min. This is fast enough at the applied strain rates for each image stack to represent a snapshot of the particle configuration at that time.

III. RESULTS

From the raw stacks of confocal images, we locate the centers of all particles in three dimensions using standard particle location software [35], run iteratively to minimize missed or doubly located particles [23]. We then convert the coordinates from units of pixels to micrometers using an experimentally calibrated conversion factor [36]. Finally, we link the particle locations over time into 3D trajectories, including trajectories that begin or end as particles near the edge move into or out of the field of view. These trajectories are the basis of all subsequent analyses.

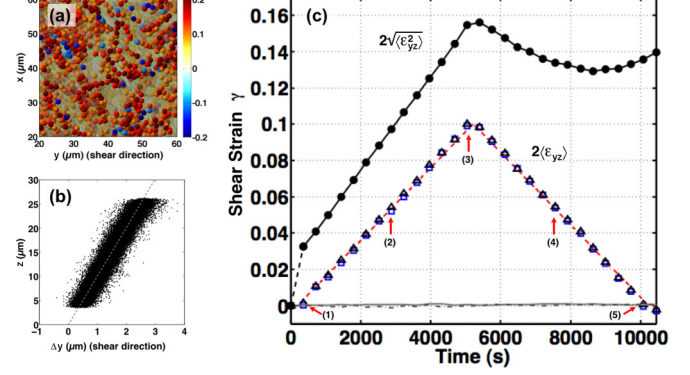


FIG. 5. (Color online) (a) Reconstruction of a small region of the colloidal glass when the applied strain was at its maximum $\gamma_{yz} = 0.1$, marked as point (3) in (c). Particles in the reconstruction are colored according to their individual strain ϵ_{yz} ; those with $|\epsilon_{yz}| \geq 0.1$ are rendered opaque. (b) Deformation profile z vs Δy at the same time, with a straight-line fit through the data. (c) Macroscopic strain measured in three ways: the applied strain (red dashed line), fitting the deformation profiles like (b) (blue squares), and the average of all the individual particle strains $2\langle\epsilon_{yz}\rangle$ (black triangles). The measured strains orthogonal to the applied strain $2\langle\epsilon_{xy}\rangle$ and $2\langle\epsilon_{xz}\rangle$ are shown as gray solid and dot-dashed lines, respectively. The rms strain $2\sqrt{\langle\epsilon_{yz}^2\rangle}$ is plotted as solid black dots.

The vector displacements of each particle's nearest neighbors between a reference time t_{ref} at the beginning of the experiment and some later time t sample the displacement field in the vicinity of each particle since t_{ref} . Nearest neighbors are defined as all particles closer to a given particle than a distance equal to the first minimum of the radial distribution function (shown in Fig. 2) and only neighbors that have moved no farther than the second neighbor shell at t are considered in strain calculations. From the neighbor displacements, we calculate [5] the local affine deformation tensor α_{ij} at each particle. By separating this tensor into its symmetric and antisymmetric parts, we obtain, respectively, the local strain ϵ_{ij} and rotation ω_{ij} tensors measured at each individual particle. A reconstruction of a small region of the glass with each particle colored according to its local ϵ_{yz} strain accumulated since the start of the experiment is shown in Fig. 5(a), with particles experiencing the largest strains drawn opaque.

During a deformation experiment, the externally applied macroscopic strain is equal to the displacement of the piezoelectric actuator over time divided by the shear gap. We measure the macroscopic shear strain γ experienced by the sample since the reference time at the beginning of the experiment, in two ways. The first is from the slope of the deformation profile, which is a plot of the displacements of the individual particles as a function of height in the sample, as in Fig. 5(b). When the deformation profile is a straight line, as it is in our experiments, the macroscopic strain is uniform throughout the sample and equal to the inverse of the slope of the line. Second, the macroscopic strain experienced by the sample is equal to twice the average local shear strain $2\langle\epsilon_{ij}\rangle$. We find close agreement between the applied strain, the macroscopic strain obtained from the deformation profiles, and the average local y - z strain over time, as shown in Fig. 5(c).

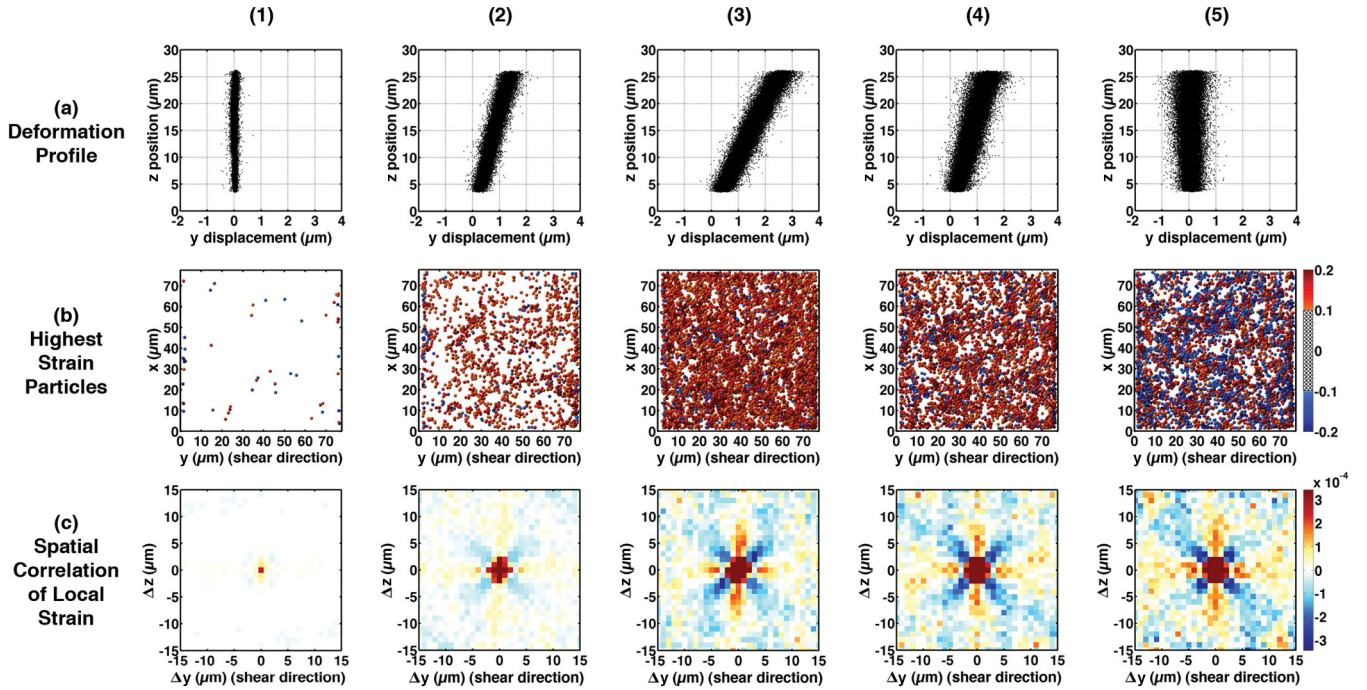


FIG. 6. (Color online) Evolution of strain and strain correlations in the colloidal glass during a shear experiment. The time and macroscopic strain corresponding to columns (1)–(5) are indicated in Fig. 5(c). Row (a) shows the deformation profiles. Row (b) shows the top-view reconstructions showing only those particles with individual strain $|\epsilon_{yz}| > 0.1$, colored according to their strain. On strain reversal, some of the regions of particles that acquire a high positive strain (red) return to a low-strain configuration and disappear from the reconstruction; others experience an irreversible local deformation and remain in a high-strain state at the end of the experiment. These are compensated for by other regions that deform in the opposite direction (blue) so that at the end the average strain is zero at time (5). Row (c) shows the y - z plane cross sections of ϵ_{yz} spatial autocorrelations, showing the evolution of the fourfold pattern that is the signature of Eshelby inclusions active in the material.

Figure 5(c) also shows that the other average shear strain components $2\langle\epsilon_{xy}\rangle$ and $2\langle\epsilon_{xz}\rangle$ remain close to zero throughout the experiments. In quiescent experiments, all components of the average local strain remain near zero over time.

The evolution of the macroscopic and local strain during deformation are shown in Fig. 6, with the reference state for the strain set the beginning of the experiment prior to any applied strain. Each row in Fig. 6 shows the results of measurements made at the times [(1)–(5)] indicated in Fig. 5(c). Row (a) shows the measured deformation profiles. Row (b) shows top-view reconstructions of only those particles with the highest magnitude strain, colored according to the local ϵ_{yz} shear strain. Note that the strains at individual particles can significantly exceed the macroscopic strain and that some even oppose the direction of the applied strain.

A similar summary of the evolution of the macroscopic and local strain during a quiescent experiment is shown in Fig. 7. This figure shows measurements of the quiescent glass at the same time intervals as in Fig. 6, although these times obviously have no particular significance in the quiescent experiment. In this experiment, the deformation profile broadens slowly, but remains vertical and centered at zero over time. We observe a coarsening and heterogeneity of the local strain field over time that is similar to that observed in the deformation experiment, but which develops more slowly.

We quantify this evolving heterogeneity of the local strain field by computing the root-mean-square (rms) strain over

time, averaged over all the particles $2\sqrt{\langle\epsilon_{yz}^2\rangle}$. During the quiescent experiment, the rms strain increases linearly with time with a slope of $0.59 \times 10^{-5} \text{ s}^{-1}$. This reflects a steady coarsening of the local strain field, corresponding to a steady broadening of the distribution of local strains about a mean macroscopic strain of zero [Fig. 7(a)].

With applied shear deformation, the rms strain evolves differently [Fig. 5(c)]. During the initial macroscopic deformation from zero to γ_{\max} , the measured rms strain experienced by the glass increases linearly at $2.6 \times 10^{-5} \text{ s}^{-1}$, significantly faster than the background thermal rate. The rms of $\epsilon_{\delta}(\mathbf{r}) = \epsilon(\mathbf{r}) - \langle\epsilon(\mathbf{r})\rangle$, the local strain minus the macroscopic strain, also increases linearly with time, at a rate of $1.8 \times 10^{-5} \text{ s}^{-1}$, three times faster than in the quiescent sample. On strain reversal, however, the rms strain actually decreases to a minimum over several percent recovered strain and then begins to rise again before the macroscopic strain returns to zero. The amount of rms strain recovery and the macroscopic deformation over which the recovery occurs are independent of strain rate at the relatively slow strain rates used in our experiments, as shown in Fig. 8.

We look for patterns in the evolution of local particle strain by computing the unnormalized three-dimensional spatial autocorrelation [9,19] of the zero-mean local strain field per particle $C_{\epsilon}(\Delta\mathbf{r}) = \langle\epsilon_{\delta}(\mathbf{r})\epsilon_{\delta}(\mathbf{r} + \Delta\mathbf{r})\rangle$, where $\Delta\mathbf{r}$ are all of the interparticle distances. The results are shown in the y - z cross section in Fig. 6(c) as they evolve over the course of the

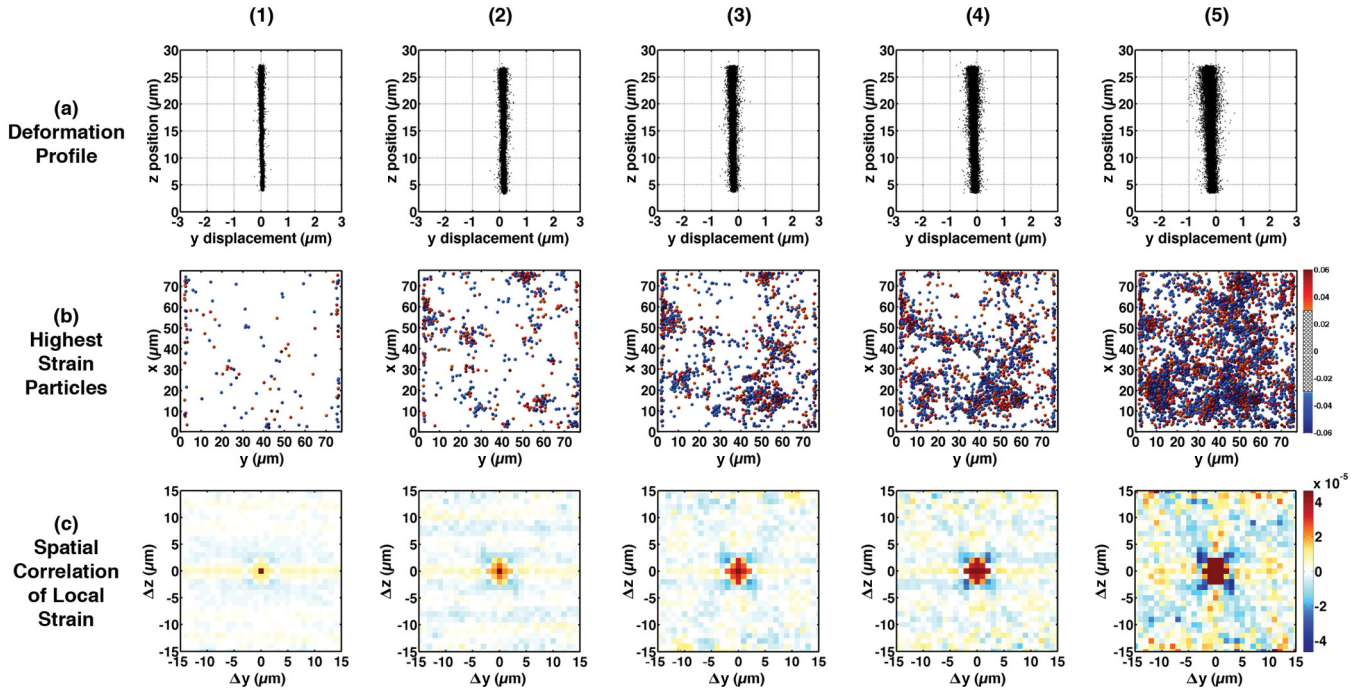


FIG. 7. (Color online) Evolution of strain and strain correlations in a quiescent colloidal glass. The time intervals are chosen to match those of Fig. 6, although these times have no particular significance in the quiescent experiment. Row (a) shows the deformation profiles, showing broadening but no deformation. Row (b) shows top-view reconstructions showing only those particles with individual strain $|\epsilon_{yz}| > 0.03$, colored according to their strain. At any time, there are equal numbers of high positive (red) and negative (blue) particles. Row (c) shows the y - z plane cross sections of ϵ_{yz} spatial strain correlations, showing the evolution of the fourfold Eshelby signature. The position axes for all figures are identical to the corresponding plots in Fig. 6. Rows (b) and (c) have smaller color scales in this figure.

experiment. The three orthogonal cross sections at maximum strain are shown in Fig. 9. For consistency, we use a fixed color scale of $\pm 0.1 \langle \epsilon_\delta \rangle_{\max}$ for all of these plots, chosen so that the pattern with the maximum dynamic range would be shown clearly.

A distinct fourfold pattern is apparent in the strain correlations. With a more sensitive color scale, the fourfold pattern is visible even in the first measurement, at which

time no macroscopic strain has yet been applied. Over time, the fourfold pattern becomes quite pronounced. In Fig. 6 we see that the fourfold pattern remains strong even after the macroscopic strain is completely reversed.

We quantify the development of the Eshelby core and surrounding pattern in the y - z strain field correlations by taking azimuthal averages in the y - z plane of the 3D spatial strain autocorrelation. These results are shown in the upper plot of Fig. 10 for the same five time points as in the previous figures. The curves in the upper plot of Fig. 10 show that the average inclusion core size increases somewhat with time during the initial positive deformation and does not reduce in size on strain reversal. By comparing the zero crossing and the position of the minimum of the azimuthal average to the analytic calculation, we estimate the average inclusion core radius to be $1.8 \mu\text{m}$, consistent with earlier observations [11]. An example of a specific inclusion with a slightly larger core radius is shown in Fig. 11.

Remarkably, the same fourfold signature appears in the spatial correlations of the local shear strain in the quiescent sample, even though there is no applied strain. Some correlations between strains in quiescent glasses have been observed [37], but the fourfold signature that we observe specifically demonstrates the presence of Eshelby-type shear transformations. These correlations are shown in the y - z cross section in Fig. 7(c) as they evolve over time and all three orthogonal cross sections at the final time are shown in Fig. 12. Again, we use a fixed color scale of $\pm 0.1 \langle \epsilon_\delta \rangle_{\max}$ for these plots; note, however, that in the quiescent sample, $\langle \epsilon_\delta \rangle_{\max}$ is almost ten times smaller than in the sheared sample and

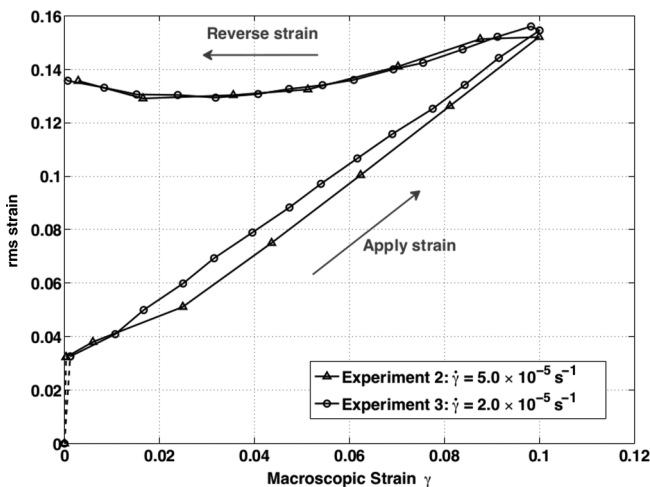


FIG. 8. Plot of the rms strain vs macroscopic strain for experiments 2 and 3. These had the same maximum strain ($\gamma_{\max} = 10.0\%$) but strain rates that differed by a factor of 2.5.

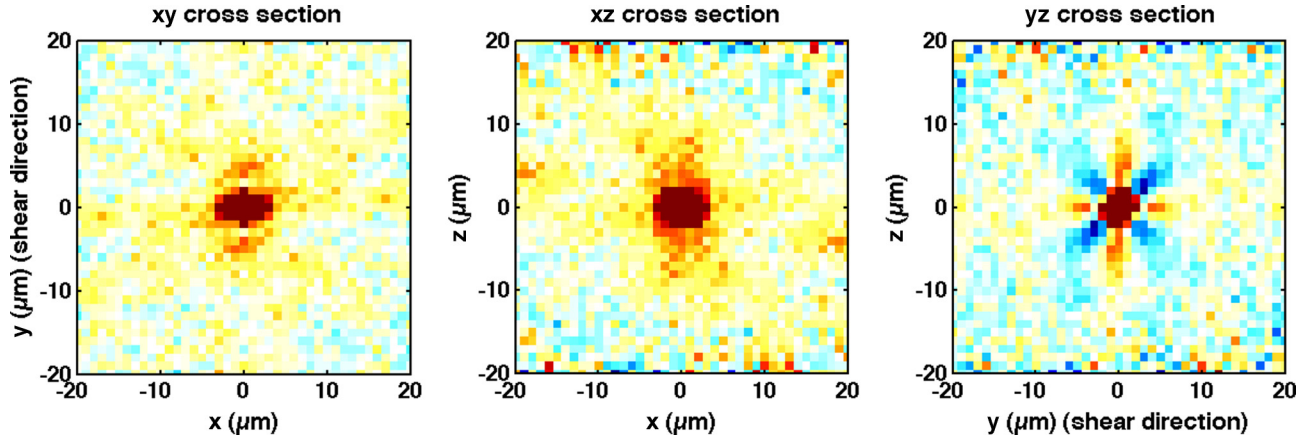


FIG. 9. (Color online) Plots of the (a) x - y , (b) x - z , and (c) y - z cross sections of the spatial autocorrelations of the ϵ_{yz} strain field at maximum applied strain ($\gamma_{\max} = 10.0\%$, $t = 5040$ s), revealing the characteristic 3D structure of an Eshelby inclusion (shown in Fig. 1).

so the color scale is accordingly different from that in the figures for the sheared sample. We also show the azimuthal averages of the strain autocorrelation for the quiescent sample in the lower plot of Fig. 10. We observe that the fourfold pattern appears more slowly than in the deformed sample, the magnitude of the correlations is smaller after the same time intervals, and the inclusion core is slightly smaller. To confirm that this signature is the result of correlated motions and cannot arise from random displacements, we computed the strain fields and spatial correlations for simulated Gaussian-distributed displacements from the positions of the reference glass (standard deviations 1%–20% of the particle diameter) and found no such signature.

IV. DISCUSSION

The deformation profiles demonstrate that the macroscopic strain experienced by the glass is homogenous during the deformation experiments. Some regions, however, undergo significantly higher than average local strain. These are the flow defects or shear transformation zones that govern plastic deformation in the glass. We can see examples of these and their strain fields directly, as in the example of Fig. 11 and in earlier work [11], but their presence is most apparent in the spatial correlations of the local strain field. The fourfold pattern of alternating positive and negative correlation surrounding the positive core in the plane of that shear strain component is the characteristic signature that these local high-strain regions transform as Eshelby inclusions. Over time, the fourfold Eshelby signature strengthens, corresponding to an increasing concentration in the material of regions that have transformed as Eshelby inclusions since the start of the experiment. That the Eshelby signature remains dominant in the correlations over time and with applied strain indicates that these inclusions are the dominant plastic deformation mechanism in the glass.

Interestingly, we observe the same fourfold Eshelby signature in quiescent glass strain field correlations. This means that the same type of shear transformations exist and are active in the quiescent glass, where only thermal energy is available to drive the transformations. However, the inclusion activation is slower than in the deformed glass and we observe significantly less motion over the same time intervals; the correlation

signature, breadth of the displacement profile, and rms strain all grow more slowly in the quiescent experiment than in its deformed counterpart. Further, without any applied strain to provide a directional bias, the purely thermally activated inclusions in the quiescent sample produce no macroscopic strain.

Deformation of a material has elastic and plastic components. Upon reversal of the strain, if the deformation were purely elastic, we would expect all of the local strain to be fully reversible and the particles to return to their initial positions. If the deformation were purely plastic, we would expect to see no reversibility; rather, the strain reversal would simply cause plastic deformation to begin immediately in the opposite direction. We observe an intermediate behavior: partial elastic recovery followed by new plastic deformation in the reverse direction. This behavior is characteristic of a material that has been loaded elastically and then driven beyond its yield strain [26] prior to strain reversal.

From the reconstructions of local strain in row (b) of Fig. 6, we see directly that the local strain is reversed in two ways. Some regions that attained a high local strain (colored red) disappear from the reconstruction as the strain is reversed [between time (3) and time (4)]. In these locations, the strain was locally *reversible* and when the applied strain was reversed the particles returned very nearly to their original configurations. In other regions, the local strain was *irreversible*; these regions retain a high positive local strain (red) even when the macroscopic strain has returned to zero. To compensate, other regions transform with high-magnitude strain in the opposite sense (blue) so that the average strain remains equal to the applied strain. As the strain is reversed, the fourfold Eshelby signature remains strong because of the irreversibly transformed regions. As plastic deformation eventually begins in the opposite direction, the new, negative inclusions also contribute positively to the spatial strain correlation [9].

The decrease in rms strain observed on strain reversal results from recovery of stored elastic displacements. Once all the stored elastic strain has been reversed, the glass is in a state of zero stress, but still has a net positive strain from the irreversible plastic deformation that it experienced after yield. In order to return to net zero macroscopic strain, the glass must undergo new plastic deformation in the reverse direction to undo this residual strain. This causes the subsequent rise in

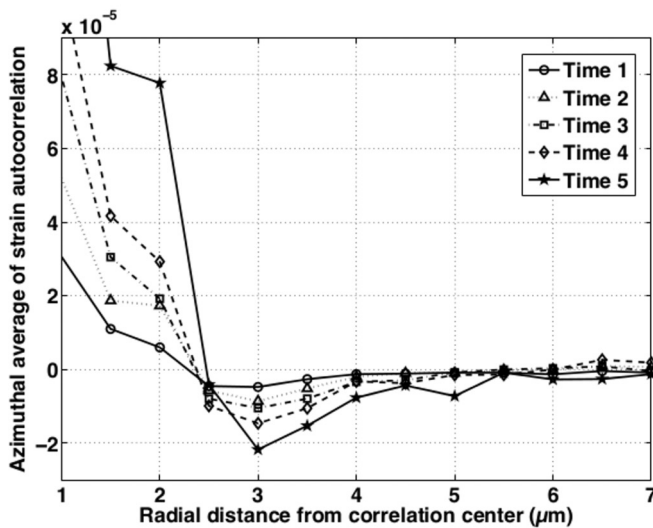
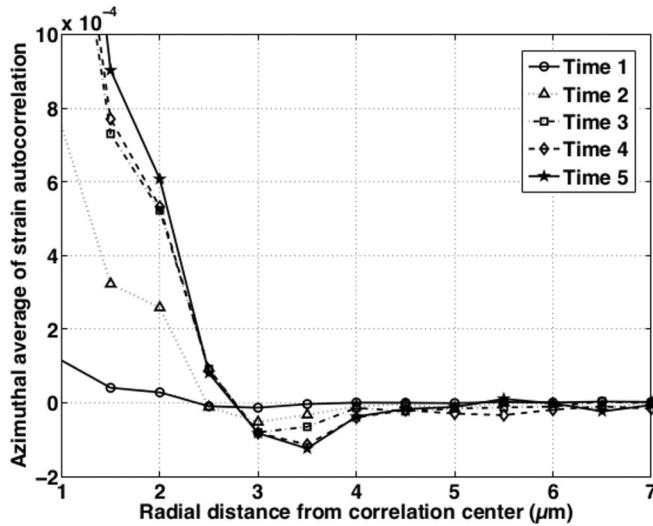


FIG. 10. Azimuthal average in the y - z plane of the spatial autocorrelation of the ϵ_{yz} strain field. The radial distance is measured from the correlation center for the sheared (top) and quiescent (bottom) samples. The times refer to Fig. 5(c). The scale of the vertical axis for the sheared plot is ten times that of the quiescent plot.

the rms strain late in the experiment as the macroscopic strain is driven to zero. The rms strain does not return to zero precisely because the material has undergone irreversible internal rearrangements that are not undone by reversing the macroscopic strain. We do not expect a perfect return to zero rms strain even below yield because there always exists some thermal background of local shear transformations, as the quiescent experiment demonstrates. However, since the maximum strain in our deformation experiments is beyond yield, the rms strain is driven well above the thermal background and does not recover even to the thermal background on strain reversal.

In the core of the inclusions, where the strains are largest, the deformation is less affine than in the surrounding matrix, where the strains are smaller. Because the strains in the matrix are more affine, it is still possible to obtain a clear fourfold

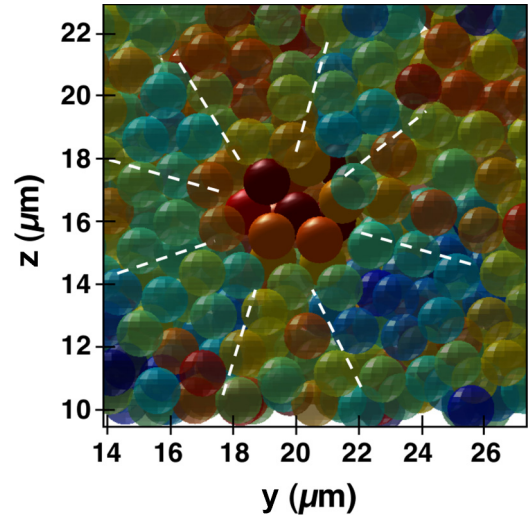


FIG. 11. (Color online) Example of an Eshelby inclusion (opaque) and its surroundings (semitransparent) reconstructed from an experiment with a hard-sphere glass deformed at slightly under $\dot{\gamma} = 10^{-5} \text{ s}^{-1}$. Particles are colored according to their local shear strain ϵ_{yz} , with red indicating high positive strain and blue indicating negative strain. Dashed lines approximately indicate the fourfold alternating positive and negative strain field surrounding the inclusion.

autocorrelation pattern, even with a considerable nonaffine deformation in the core.

V. CONCLUSION

We followed the 3D trajectories of roughly 50 000 individual particles in colloidal glasses under conditions of quiescence and applied shear deformation. We measured the macroscopic and local strain in the glasses and observed an evolving fourfold pattern in spatial autocorrelations of the local strain field, both with and without deformation. These fourfold patterns indicate that the dominant deformation mechanisms in the glass are shear transformation zones that behave as Eshelby inclusions: local regions of high plastic strain that couple elastically to the surrounding material. These inclusions exist and are active even in the absence of applied strain; the available thermal energy can be sufficient to activate them, although without any directional bias they contribute no macroscopic strain.

With applied strain, we find that the Eshelby signature evolves more quickly. The applied shear stress biases the population of inclusions in the direction of the applied strain, so they contribute to the macroscopic deformation. When the glass is strained beyond yield, many of the local transformations are irreversible and result in permanent plastic deformation. These contribute a net positive strain from within the material. The result is a permanent fourfold Eshelby signature in the strain correlations and an rms strain that remains above the thermal background even when the macroscopic strain has returned to zero. As we drive the material back to zero macroscopic strain, these irreversibly transformed regions are compensated for by the activation of inclusions with a negative internal strain. The average diameter of the inclusions at 10% shear strain is 2.3 particle diameters.

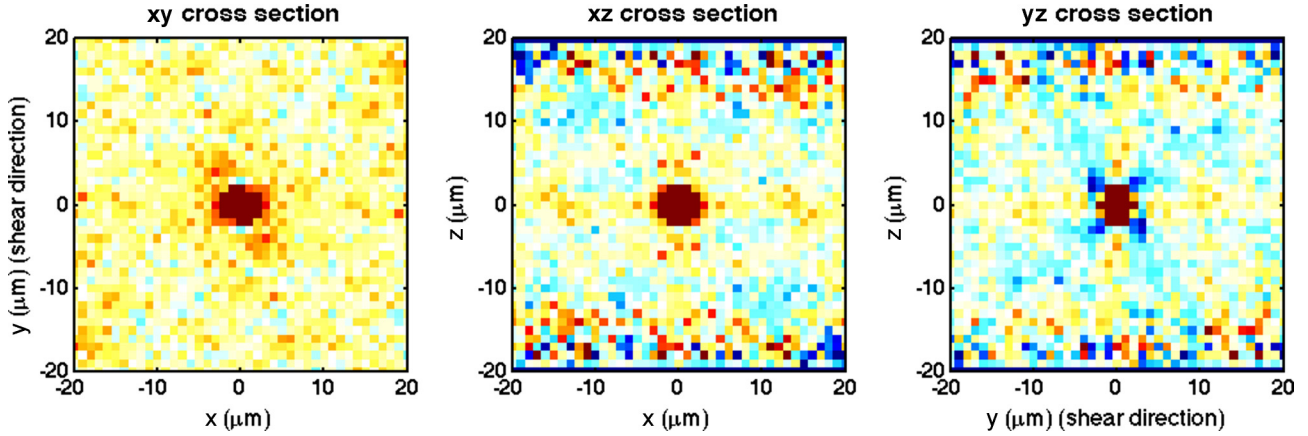


FIG. 12. (Color online) Plots of the (a) x - y , (b) x - z , and (c) y - z cross sections of the spatial autocorrelations of the ϵ_{yz} strain field at the longest time interval [corresponding to Fig. 7, column (5)]. The correlations in the quiescent glass exhibit the same characteristic 3D structure as those for the calculated strain of an Eshelby inclusion (Fig. 1).

The rms strain also increases faster with applied strain than it would just from the available thermal energy; on strain reversal, the rms strain drops to a local minimum over several percent strain recovery until the glass attains a state of zero stress. The drop in rms strain corresponds to a decrease in the energy stored in the strain field; the elastic energy that was stored in the glass during its initial, elastic loading is being recovered. Finally, the rms strain starts to rise again as the glass begins to deform plastically in the opposite direction. Because this is the only way that net zero macroscopic strain can be reached, it causes a new increase in the rms strain since the negative-strain inclusions contribute positively to the rms strain.

The regions that can transform as Eshelby inclusions exist and can be thermally activated in a quiescent glass. We have also directly observed additional examples in our experiments of particle clusters that directly exhibit the strain signature of the Eshelby fourfold pattern, such as the one shown in Fig. 11.

ACKNOWLEDGMENTS

This work was supported by the National Science Foundation through the Harvard MRSEC (Contract No. DMR-0820484) and by Contract No. DMR-1206765. We thank John Hutchinson for help with the mechanics of the Eshelby inclusion, Roderick W. Jensen for assistance in preparing Figs. 6 and 7, and Peter Schall for many useful discussions.

APPENDIX: ANALYTIC STRAIN FIELDS

Eshelby calculates the three-dimensional displacements for a spherical inclusion with an unconstrained transformation shear strain $\epsilon_{yz}^T = \gamma/2$ and inclusion radius a in an

isotropic elastic medium with dimensionless elastic constant $c = 1/4(4 - 5\nu)$. Here ν is Poisson's ratio, taken to be $1/3$ for this colloidal glass [11, 13].

The shear strain inside the inclusion when it is embedded in the elastic matrix is

$$\epsilon_{yz}^0 = \gamma \frac{4 - 5\nu}{15(1 - \nu)}. \quad (\text{A1})$$

For such an inclusion, the displacements at distances $r = \sqrt{x^2 + y^2 + z^2}$ outside the inclusion are

$$u_x = \epsilon_{yz}^0 a^3 \left\{ 6c(r^2 - a^2) \left(\frac{5xyz}{r^7} \right) \right\}, \quad (\text{A2})$$

$$u_y = \epsilon_{yz}^0 a^3 \left\{ \frac{z}{r^3} + 6c(r^2 - a^2) \left(\frac{5y^2z}{r^7} - \frac{z}{r^5} \right) \right\}, \quad (\text{A3})$$

$$u_z = \epsilon_{yz}^0 a^3 \left\{ \frac{y}{r^3} + 6c(r^2 - a^2) \left(\frac{5yz^2}{r^7} - \frac{y}{r^5} \right) \right\}. \quad (\text{A4})$$

This result holds if the elastic constants are the same for the matrix and the inclusion. The full deformation tensor is $\alpha_{ij} = \frac{\partial u_i}{\partial r_j}$ and the strain tensor ϵ_{ij} is the symmetric part of α_{ij} . The resulting shear strain outside of the inclusion core, expressed in cylindrical coordinates, is

$$\begin{aligned} \epsilon_{yz}(r, \theta, x) = & \frac{a^3 \epsilon_{yz}^0}{4(r^2 + x^2)^{9/2}} \{ 9a^2 cr^4 - (2 + 3c)r^6 \\ & + 9cr^2(-8a^2 + 5r^2)x^2 + 6[r^2 + 4c(a^2 + r^2)]x^4 \\ & + 4(1 - 6c)x^6 + 15cr^4[-7a^2 \\ & + 5(r^2 + x^2)] \cos(4\theta) \}, \end{aligned} \quad (\text{A5})$$

where as above $\mathbf{r}(y, z)$ is the position vector from the center of the inclusion and $\theta = \cos^{-1}(z/r)$.

[1] F. Spaepen, *Acta Metall.* **25**, 407 (1977).

[2] A. S. Argon, *Acta Metall.* **27**, 47 (1979).

[3] G. Picard, A. Ajdari, F. Lequeux, and L. Bocquet, *Eur. Phys. J. E* **15**, 371 (2004).

[4] J. S. Langer, *Phys. Rev. E* **85**, 051507 (2012).

[5] M. L. Falk and J. S. Langer, *Phys. Rev. E* **57**, 7192 (1998).

[6] C. E. Maloney and A. Lemaître, *Phys. Rev. E* **74**, 016118 (2006).

- [7] A. Tanguy, F. Leonforte, and J.-L. Barrat, *Eur. Phys. J. E* **20**, 355 (2006).
- [8] A. Lemaître and C. Caroli, *Phys. Rev. Lett.* **103**, 065501 (2009).
- [9] J. Chattoraj and A. Lemaître, *Phys. Rev. Lett.* **111**, 066001 (2013).
- [10] A. L. Greer and E. Ma, *Mater. Res. Bull.* **32**, 611 (2007).
- [11] P. S. Schall, D. A. Weitz, and F. Spaepen, *Science* **318**, 1895 (2007).
- [12] V. Prasad, D. Semwogerere, and E. R. Weeks, *J. Phys.: Condens. Matter* **19**, 113102 (2007).
- [13] K. E. Jensen, D. Pennachio, D. Recht, D. A. Weitz, and F. Spaepen, *Soft Matter* **9**, 320 (2013).
- [14] P. Schall, I. Cohen, D. A. Weitz, and F. Spaepen, *Science* **305**, 1944 (2004).
- [15] P. Schall, I. Cohen, D. A. Weitz, and F. Spaepen, *Nature (London)* **440**, 319 (2006).
- [16] P. Schall and F. Spaepen, in *Dislocations in Solids*, edited by J. P. Hirth and L. Kubin (Elsevier, New York, 2010), p. 233.
- [17] P. Schall and F. Spaepen, *Int. J. Mater. Res.* **97**, 958 (2006).
- [18] M. C. M. Persson Gulda, Ph.D. thesis, Harvard University, 2013.
- [19] V. Chikkadi, G. Wegdam, D. Bonn, B. Nienhuis, and P. Schall, *Phys. Rev. Lett.* **107**, 198303 (2011).
- [20] J. D. Eshelby, *Proc. R. Soc. London Ser. A* **241**, 376 (1957).
- [21] J. D. Eshelby, *Proc. R. Soc. London Ser. A* **252**, 561 (1959).
- [22] We purchase specially filtered Sicaster plain particles from Micromod (www.micromod.de). According to the manufacturer, the particles have an average diameter $2\bar{R} = 1.55 \mu\text{m}$. The polydispersity is measured by fitting the first peak of the radial distribution function from a densely packed sample and deconvolving to obtain the particle size distribution.
- [23] K. E. Jensen, Ph.D. thesis, Harvard University, 2013. The amorphous templates are described on pp. 49–53 and the iterative particle locating algorithm is described on pp. 25–27.
- [24] J. L. Finney, *Proc. R. Soc. London Ser. A* **319**, 479 (1970).
- [25] N. Nakamura, K. E. Jensen, D. A. Weitz, and F. Spaepen (unpublished).
- [26] Note that we use the conventional mechanical testing definition of yield, which refers to the onset of irreversible deformation. This differs from the rheological definition of yield, which instead refers to the strain at which the viscous response of the material begins to dominate over the elastic, that is, when the loss modulus G'' exceeds the storage modulus G' .
- [27] W. L. Johnson and K. Samwer, *Phys. Rev. Lett.* **95**, 195501 (2005).
- [28] G. Petekidis, A. Moussaïd, and P. N. Pusey, *Phys. Rev. E* **66**, 051402 (2002).
- [29] L. Mohan, C. Pellet, M. Cloitre, and R. Bonnecaze, *J. Rheol.* **57**, 1023 (2013).
- [30] E. D. Knowlton, D. J. Pine, and L. Cipelletti, *Soft Matter* **10**, 6931 (2014).
- [31] D. Fiocco, G. Foffi, and S. Sastry, *Phys. Rev. E* **88**, 020301(R) (2013).
- [32] C. F. Schreck, R. S. Hoy, M. D. Shattuck, and C. S. O'Hern, *Phys. Rev. E* **88**, 052205 (2013).
- [33] N. Perchikov and E. Bouchbinder, *Phys. Rev. E* **89**, 062307 (2014).
- [34] See Supplemental Material at <http://link.aps.org/supplemental/10.1103/PhysRevE.90.042305> for video.
- [35] Y. Gao and M. L. Kilfoil, *Opt. Express* **17**, 4685 (2009). We use the locating software described in this publication, which is available under “MATLAB 3D feature finding algorithms” at <http://people.umass.edu/kilfoil/downloads.html>.
- [36] K. E. Jensen, D. A. Weitz, and F. Spaepen, *Rev. Sci. Instrum.* **84**, 016108 (2013).
- [37] Y. Rahmani, R. Koopman, D. Denisov, and P. Schall, *Phys. Rev. E* **89**, 012304 (2014).